ChemComm

COMMUNICATION

View Article Online
View Journal | View Issue

Cite this: *Chem. Commun.*, 2020, **56**, 1589

Received 28th November 2019,
Accepted 3rd January 2020

DOI: 10.1039/c9cc09270f

rsc.li/chemcomm

Single crystal structure and opto-electronic properties of oxidized Spiro-OMeTAD†

Wei Zhang, [a] Linqin Wang,[b] Yu Guo,[a] Biaobiao Zhang, [b] Valentina Leandri,[a] Bo Xu, [b] Zhuofeng Li, [a] James M. Gardner, [a] Licheng Sun [bc] and Lars Kloo *[a]

Single crystals of Spiro(TFSI)$_2$ were grown, the optical and electronic properties were characterized and compared with neutral Spiro-OMeTAD. Density-functional theory was used to get insights into binding and band structure properties. The flat valence bands indicate a rather limited orbital overlap in Spiro(TFSI)$_2$.

As one of the most widely used organic hole-transport materials in solid-state, mesoscopic solar cells, 2,2′,7,7′-tetrakis[*N*,*N*-di(4-methoxyphenyl)amino]-9,9′-spirobifluorene (Spiro-OMeTAD) was first reported by Salbeck in blue electroluminescence devices[1] and then applied by Bach and co-workers in solar cells in 1998.[2] Since then, thousands of studies have been conducted involving Spiro-OMeTAD as hole-transport material (HTM), especially in solid-state dye-sensitized solar cells[3] (ssDSSCs) and perovskite solar cells (PSCs).[4] Nowadays, although several alternatives have been reported,[5,6] Spiro-OMeTAD is still considered as one of the best materials and has become the reference for perovskite solar cells.[7–9] Chemical doping to oxidize Spiro-OMeTAD is very important to improve the hole mobility and conductivity with respect to the pristine material.[10–12] With doping, oxidized Spiro-OMeTAD, such as Spiro$^+$ and/or Spiro^{2+} (denoting singly and doubly oxidized Spiro-OMeTAD), is formed and the charge-carrier density is increased. However, it is unclear what is actually formed in the doping process.[13,14] Exact knowledge becomes extremely important when aiming to assign for instance the light-absorption peaks of oxidized Spiro-OMeTAD. Some previous studies show that Spiro$^+$ and Spiro^{2+} display very similar absorption features but different absorption intensities.[15] However, some studies indicate that the light-absorption peaks for Spiro$^+$ and Spiro^{2+} should be different, and the peak observed at around 521 nm should be assigned to Spiro$^+$, while the peak observed at around 691 nm should be attributed to Spiro^{2+}.[16,17] In order to clarify this question, determining the absorption peaks directly by dissolving the single crystals of oxidized Spiro-OMeTAD would be the best option. Moreover, understanding of the structure of oxidized Spiro-OMeTAD, as well as its optical and electronic properties, will give insights into hole-transport mechanisms in doped Spiro-OMeTAD.

The structure of Spiro-OMeTAD was not reported until 2016 by Bakr *et al.*, on the basis of single crystals obtained by an anti-solvent method.[18] The resulting crystal structure shows a triclinic lattice system belonging to the $P\bar{1}$ space group. It was found that the Spiro-OMeTAD molecules form dimers in the structure, and one of the fluorenes is slightly curved. The closest distance between two fluorene rings is estimated to be about 3.8 Å, which is close enough to provide significant electronic coupling between stacked conjugated fragments. However, the steric hindrance between the outer fragments of each molecule prevents the formation of a continuous π–π stacking pattern, which eventually results in a low hole mobility and conductivity. Very recently, a similar method involving ethyl acetate was used to grow Spiro-OMeTAD crystals up to several millimeters.[19] The properties of the crystals and the films were compared, and it was found that the crystal displays much higher conductivity and hole mobility. This was attributed to the better interphenylene π–π stacking in the Spiro-OMeTAD crystals. Although oxidation was mentioned in their work, neither the structure of partially oxidized Spiro-OMeTAD nor the structure of fully oxidized Spiro-OMeTAD were reported.

Herein, we report the structure of an oxidized Spiro-OMeTAD, Spiro(TFSI)$_2$. Results from density-functional theory (DFT) calculations offer insights both regarding chemical bonding and band structure of the compounds. Further, by dissolving the crystals in acetonitrile, the UV/visible absorption and chemical stability of Spiro^{2+} in solution can be investigated. The redox potential, hole

[a] *Department of Chemistry, Applied Physical Chemistry, KTH Royal Institute of Technology, SE-10044 Stockholm, Sweden. E-mail: lakloo@kth.se*
[b] *Department of Chemistry, Organic Chemistry, KTH Royal Institute of Technology, SE-10044 Stockholm, Sweden*
[c] *State Key Laboratory of Fine Chemicals, DUT-KTH Joint Research Center on Molecular Devices, Dalian University of Technology (DUT), 116024 Dalian, China*

† Electronic supplementary information (ESI) available: Experimental details, optical image of the single crystal, EPR spectrum, ^{19}F NMR spectrum, XRD patterns, SEM image, electrolysis of Spiro-OMeTAD, crystallographic data, Spiro(TFSI)$_2$ dimers, unit cell parameters, frontier orbitals, electronic band structures of Spiro-OMeTAD and Spiro(TFSI)$_2$, molar extinction coefficients, UV/visible absorption of Spiro(TFSI)$_2$ in fresh and after aging. CCDC 1965026. For ESI and crystallographic data in CIF or other electronic format see DOI: 10.1039/c9cc09270f

mobility and conductivity of Spiro(TFSI)$_2$ were also studied and compared with Spiro-OMeTAD.

Spiro(TFSI)$_2$ was synthesized by reacting Spiro-OMeTAD with silver bis(trifluoromethanesulfonyl)imide (AgTFSI) according to a reported procedure,[20] synthetic route is shown in Scheme S1 (ESI†). The structure was verified by both elemental analysis (EA) and nuclear magnetic resonance (NMR) spectroscopy. As expected, the elemental contents correspond well with the expected ratios in the compound. However, the proton NMR spectra could not be successfully obtained for Spiro(TFSI)$_2$ in deuterated dimethyl sulfoxide solution due to the paramagnetic property of the cation. The Spiro^{2+} looses its two electrons from the two separate fluorene rings, which can be regarded as electronically orthogonal, and therefore an open-shell triplet state of the cation in Spiro(TFSI)$_2$ is obtained. DFT calculations were conducted in order to compare the energy difference between the Spiro^{2+} singlet state and the corresponding triplet state. It was found that the triplet is 15.5 kcal mol^{-1} lower in energy than the singlet state and thus a more likely product of double oxidation. The triplet state of Spiro^{2+} was also confirmed from electron paramagnetic resonance (EPR) spectroscopy results (Fig. S1, ESI†), which are in accordance with previously reported results on Spiro(PF$_6$)$_2$.[21] Although informative proton NMR spectra are not possible to obtain, the fluorine NMR spectra from the anions were obtainable. As a result, only one peak at −78.6 ppm was observed, and since a fast exchanging system involving TFSI$^-$ appears unlikely, a single chemical environment for fluorine atoms is a more likely case for Spiro(TFSI)$_2$. A typical ^{19}F NMR spectrum is shown in Fig. S2 (ESI†).

The structure of Spiro(TFSI)$_2$ (CCDC deposit number 1965026†) was investigated using single-crystal X-ray diffraction, the crystallographic data are shown in Table S1 (ESI†). Fig. S3 (ESI†) shows the optical image of a single crystal with octahedral shape. Comparison between the geometries of molecular Spiro-OMeTAD in its neutral (CCDC deposit number 1475944)[18] and its oxidized forms shows rather modest differences in the geometric structure. The spirobifluorene core geometry responds to the oxidation with a decrease of the C7–C7′ bond distance (indicated in Scheme 1) that connects the two phenyl rings in the same fluorene unit (from 1.469 Å for the neutral species to 1.434 Å for Spiro^{2+}). The distance of C–N bonds including C$_4$–N$_8$, N$_8$–C$_9$ and N$_8$–C$_{10}$ in the triphenylamine group also decrease slightly, together with the lower angles Φ observed (from 121.63° to 121.09°) and θ (from 115.54° to 114.68°). The dihedral angle Φ characterizes the out-of-plane distortion of the methoxy-group-substituted (MeO–) phenyls with respect to the fluorene moieties, while the angle θ describes disturbance of the MeO–group from the outermost molecular environment with respect to phenyl rings. The decrease in C–N bond distances and angles observed are not the same as a prediction from calculations,[15] in which effects of anions and crystal packing may be overlooked. Details of geometrical parameters in Spiro-OMeTAD and Spiro(TFSI)$_2$ are shown in Table 1.

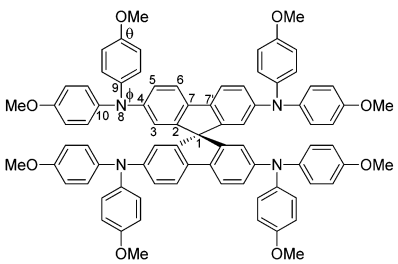

Scheme 1 Molecular structure and labels of the main geometrical parameters of Spiro-OMeTAD molecule/ions.

Table 1 Main geometrical parameters of Spiro-OMeTAD and Spiro(TFSI)$_2$ from single-crystal data[a,b]

Parameters	Spiro-OMeTAD	Spiro(TFSI)$_2$
C$_1$–C$_2$	1.525	1.523
C$_2$–C$_3$	1.380	1.372
C$_2$–C$_7$	1.400	1.419
C$_3$–C$_4$	1.400	1.417
C$_4$–C$_5$	1.403	1.410
C$_4$–N$_8$	1.414	1.393
C$_5$–C$_6$	1.387	1.377
C$_6$–C$_7$	1.391	1.402
C$_7$–C$_7$	1.469	1.434
N$_8$–C$_9$	1.423	1.418
N$_8$–C$_{10}$	1.431	1.427
Φ	121.63	121.09
θ	115.54	114.68

[a] Bond distances in Å and angles in degrees. [b] See Scheme 1 for labels.

Spiro-OMeTAD crystallized in the triclinic $P\bar{1}$ (2) space group, whereas Spiro(TFSI)$_2$ crystallizes in the orthorhombic *Fddd* (70) space group. As shown in Fig. 1, the structure of Spiro(TFSI)$_2$ does not show strong twisting in the central fluorene rings. Also, because of the anions involved, the Spiro^{2+} molecules have been pushed away from each other and no direct contacts between the fluorene rings can be observed. The closest distance between two Spiro^{2+} ions is around 3.8 Å, as shown in Fig. S4 (ESI†). This contact does not represent a π–π interaction, and the distance is too long for carbon-orbital overlap and thus will not likely facilitate intermolecular charge transfer in Spiro(TFSI)$_2$ crystals. It is not possible to directly deduce which atoms that loose electrons from the structural data, as the position of TFSI$^-$ does not communicate such information. This is further complicated by structural disorder of the anions. The unit cell of Spiro(TFSI)$_2$ is much larger than that of Spiro-OMeTAD, details are shown in Table S2 (ESI†). The powder X-ray diffraction pattern of Spiro(TFSI)$_2$ compared with a simulation from single crystal-data are quite similar, as shown in Fig. S5 (ESI†).

DFT calculations were performed in order to compare the frontier orbitals of the molecular structures obtained from diffraction for both Spiro-OMeTAD and Spiro^{2+}, as shown in Fig. S6 (ESI†). The highest occupied molecular orbital (HOMO) and lowest unoccupied molecular orbital (LUMO) of Spiro^{2+} show a very small difference between the two experimental and theoretical structures. The energy of the HOMO of Spiro^{2+} is around −9.9 eV, whereas the energy of the LUMO is −4.2 eV (0.1 eV less negative for the theoretically optimized Spiro^{2+}). The differences in orbital energies for Spiro-OMeTAD are larger. The difference in HOMO energy of Spiro-OMeTAD is around 0.1 eV, and the difference in LUMO energy is as high as 0.3 eV. The larger difference for Spiro-OMeTAD is due to twisting of one of the fluorenes in the structure arising from inter-molecular π–π interactions. The HOMO and HOMO−1, which are expected to dominate hole transport, are nearly degenerate with respect to energy and with wave functions localized on one of the two orthogonal fluorene rings.

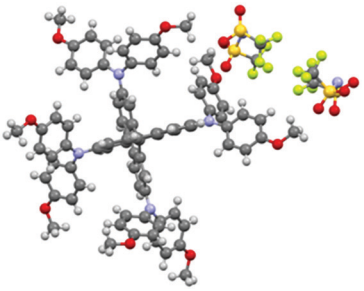

Fig. 1 Structure of Spiro(TFSI)$_2$ (disorder of the anions removed).

A similar phenomenon is also found for Spiro^{2+}, as indicated in Table S3 (ESI†).

The electronic band structures of Spiro-OMeTAD and Spiro(TFSI)$_2$ were investigated and are shown in Fig. S7 (ESI†). Details of the top of valence bands of Spiro-OMeTAD are shown in Fig. 2. As observed, the valence bands in Spiro-OMeTAD are not flat when using a reasonable energy resolution, indicating effective interaction between the molecular orbitals in the Spiro-OMeTAD dimers noted in the crystal structure unit cell. A notable feature for Spiro(TFSI)$_2$ is that the bands are quite flat in the whole Brillouin zone, indicating that Spiro(TFSI)$_2$ films are less likely to be characterized by significantly overlapping molecular orbitals. Considering the close spacing of the energy levels of molecular orbitals in both Spiro-OMeTAD and Spiro(TFSI)$_2$, the charge transport in a partially oxidized Spiro-OMeTAD is expected to be dominated by hopping mechanism mediated by orbital overlap,[22] which is different from most inorganic semiconductors. The bandgap of Spiro-OMeTAD suggested from band structure calculations is quite large, higher than 6 eV. However, for trivial reasons it decreases significantly after oxidation to a level less than 0.1 eV, indicating clear consequences for the light absorption.

In order to investigate the redox potential of Spiro(TFSI)$_2$, cyclic voltammetry (CV) was performed in dichloromethane (DCM) solution. A typical cyclic voltammogram is shown in Fig. 3(a). As expected, the Spiro(TFSI)$_2$ shows almost the same redox potentials as neutral Spiro-OMeTAD. The first oxidation peak corresponds to reaction (1), in which Spiro-OMeTAD looses its first electron and form Spiro$^+$. The second oxidation peak at 0.15 V *vs.* Fc/Fc$^+$ corresponds to reaction (2), where Spiro$^+$ further looses one electron and form Spiro^{2+}. The third oxidation peak gives information about the redox potential for Spiro^{2+}, which is 0.35 V *vs.* Fc/Fc$^+$. This is a two-electron process as represented in reaction (3). A previous paper assigns this peak to Spiro^{2+} to Spiro^{3+}.[20] However, we confirm our assignments by a charge estimate from electrolysis of Spiro-OMeTAD at 1.1 V *vs.* Ag/AgCl; the details are shown in Fig. S8 (ESI†).

$$\text{Spiro-OMeTAD}-e^- \rightarrow \text{Spiro}^+ \quad (1)$$

$$\text{Spiro}^+-e^- \rightarrow \text{Spiro}^{2+} \quad (2)$$

$$\text{Spiro}^{2+}-2e^- \rightarrow \text{Spiro}^{4+} \quad (3)$$

In order to investigate the optical properties of oxidized Spiro-OMeTAD, UV/visible absorption spectra of Spiro(TFSI)$_2$ were recorded by dissolving single crystals in acetonitrile. Absorption spectra of Spiro-OMeTAD are also provided for comparison. As shown in Fig. 3(b). The absorption peak at 377 nm with a molar extinction coefficient of 7.53 × 10^4 cm^{-1} M^{-1} is characteristic for Spiro-OMeTAD, and the peak originates from transitions from HOMO/HOMO−1 to both LUMO and LUMO+1 of partial charge-transfer character. This peak is shifted to 371 nm with strongly reduced intensity after Spiro^{2+} is formed, the molar extinction coefficient is lower, 1.74 × 10^4 cm^{-1} M^{-1}. Upon oxidation, new peaks at around 521, 691, 908 and 1527 nm emerge, corresponding to π–π*, n–π* and other transitions. The result is similar to those described in a previous report.[20] The investigation of UV/visible absorption features of Spiro(TFSI)$_2$ shows that Spiro^{2+} gives rise to absorption features in the whole range of measurement (300–2000 nm), which is in accordance with the small bandgap predicted by the electronic band structures. The details of the absorption positions as well as intensities of Spiro-OMeTAD and Spiro(TFSI)$_2$ are listed in Table S4 (ESI†). The stability of Spiro(TFSI)$_2$ in acetonitrile was investigated and found to be poor. Fig. S9 (ESI†) shows the UV/visible absorption spectrum of freshly prepared Spiro(TFSI)$_2$ and the corresponding spectrum after aging for two months. All peaks caused by the initial oxidation and at wavelengths longer than 450 nm have disappeared and the peak intensity at around 377 nm has increased in intensity after aging. This indicates that Spiro(TFSI)$_2$ is unstable in solution and will slowly degrade into Spiro-OMeTAD. The reasons are not clear but Spiro^{2+} is quite oxidative and reactions with the solvent or impurities in dilute solution may take place. This observation may also explain why oxidized Spiro-OMeTAD bleaches after storing for several days and the low device stability observed in most studies.

The hole mobility and conductivity of Spiro(TFSI)$_2$ were also investigated and compared with Spiro-OMeTAD. As shown in Fig. 4(a), the hole mobility of Spiro-OMeTAD dramatically increases from 1.62 × 10^{-4} cm^2 V^{-1} s^{-1} to 2.19 × 10^{-3} cm^2 V^{-1} s^{-1}

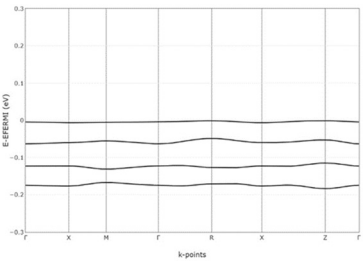

Fig. 2 Top valence bands of Spiro-OMeTAD. The crystallographic coordinates of high-symmetry points in the first Brillouin zone.

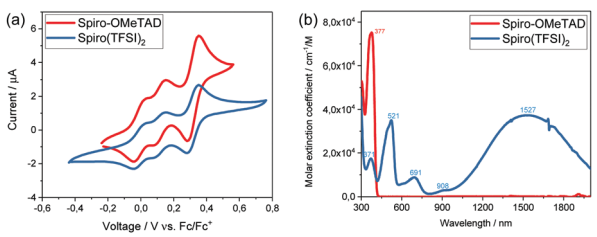

Fig. 3 (a) Cyclic voltammograms and, (b) UV/visible absorption spectra of Spiro-OMeTAD and Spiro(TFSI)$_2$ in acetonitrile solution.

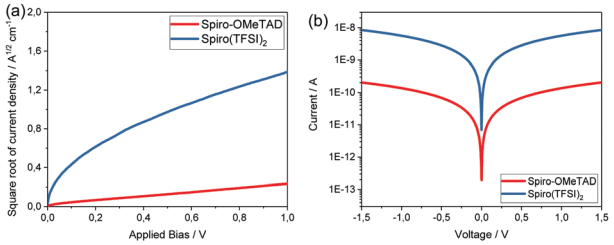

Fig. 4 (a) The hole mobility and, (b) the conductivity of $Spiro(TFSI)_2$ and Spiro-OMeTAD.

after oxidation. The same increase was observed regarding conductivity (Fig. 4(b)), the neutral Spiro-OMeTAD shows a conductivity around 7.77×10^{-7} S cm^{-1}, while the $Spiro(TFSI)_2$ displays a conductivity of 2.89×10^{-5} S cm^{-1}; same level as reported by most studies on Spiro-OMeTAD doped with LiTFSI.[23] As already indicated in the electronic band structures, orbital overlap is expected to be small between adjacent $Spiro^{2+}$ molecules in the crystal structure, and thus the higher hole mobility and conductivity in $Spiro(TFSI)_2$ can probably be linked to the ionic character of the compound. The improved conductivity deriving from the increased charge carrier density caused by doping and a partially oxidized Spiro-OMeTAD takes place in a molecular packing most likely resembling that in Spiro-OMeTAD.

One of the possible applications of $Spiro(TFSI)_2$ is as p-type dopant for organic hole-transport materials. $Spiro(TFSI)_2$ itself shows a rather good film quality, as indicated in Fig. S10 (ESI†). Previous work by McGehee and co-workers has shown that the compound can work as a good dopant for Spiro-OMeTAD. At high doping amounts, LiTFSI could in fact be avoided.[20] Very recently, work from Bach *et al.* has boosted device PCEs to over 19% in the absence of LiTFSI together with an increased device stability attributed to a more hydrophobic HTM layer.[24]

In summary, single crystals of doubly oxidized Spiro-OMeTAD were grown and structurally characterized. Based on the structure information, frontier orbitals and electronic band structures were modelled and compared with neutral Spiro-OMeTAD. Molecular orbital overlap together with close energy level spacing in Spiro-OMeTAD and $Spiro(TFSI)_2$ indicate that electron hopping may constitute the main transport mechanism for hole transport in doped Spiro-OMeTAD. The UV/visible absorption spectra show that $Spiro^{2+}$ absorb light up to more than 2000 nm. Previous reports assign the observed absorption peak at 521 nm to $Spiro^{+}$ and the peak at 691 nm to $Spiro^{2+}$, and the present study shows this assignment to be incorrect. Furthermore, considering the positive redox potential of $Spiro(TFSI)_2$, the compound may work efficiently as p-type dopant for many organic HTMs. Our work brings insights into the fundamental transport mechanisms in doped Spiro-OMeTAD and as well shows the potential of applying organic salts as p-type dopant for organic and metal–organic HTMs.

We acknowledge the Swedish Energy Agency and the Swedish Research Council for funding support. The authors thank Prof. Lars Eriksson for help during structure refinement and Dr. Zhen Wang for recording the SEM images. The authors acknowledge the National Supercomputer Centre at Linköping University for computation resources (SNIC 2018/7-57 and SNIC 2018/7-62). The authors W. Zhang and L. Wang thank the China Scholarship Council (CSC) for financial support.

Conflicts of interest

There are no conflicts to declare.

Notes and references

1 J. Salbeck, N. Yu, J. Bauer, F. Weissörtel and H. Bestgen, *Synth. Met.*, 1997, **91**, 209–215.
2 U. Bach, D. Lupo, P. Comte, J. E. Moser, F. Weissörtel, J. Salbeck, H. Spreitzer and M. Grätzel, *Nature*, 1998, **395**, 583–585.
3 Z. Shen, B. Xu, P. Liu, Y. Hu, Y. Yu, H. Ding, L. Kloo, J. Hua, L. Sun and H. Tian, *J. Mater. Chem. A*, 2017, **5**, 1242–1247.
4 Z. Hawash, L. K. Ono and Y. Qi, *Adv. Mater. Interfaces*, 2018, **5**, 1700623.
5 N. Arora, M. I. Dar, A. Hinderhofer, N. Pellet, F. Schreiber, S. M. Zakeeruddin and M. Grätzel, *Science*, 2017, **358**, 768–771.
6 N. J. Jeon, H. Na, E. H. Jung, T.-Y. Yang, Y. G. Lee, G. Kim, H.-W. Shin, S. Il Seok, J. Lee and J. Seo, *Nat. Energy*, 2018, **3**, 682–689.
7 B. Xu, D. Bi, Y. Hua, P. Liu, M. Cheng, M. Grätzel, L. Kloo, A. Hagfeldt and L. Sun, *Energy Environ. Sci.*, 2016, **9**, 873–877.
8 A. Connell, Z. Wang, Y.-H. Lin, P. C. Greenwood, A. A. Wiles, E. W. Jones, L. Furnell, R. Anthony, C. P. Kershaw, G. Cooke, H. J. Snaith and P. J. Holliman, *J. Mater. Chem. C*, 2019, **7**, 5235–5243.
9 L. Wang, J. Zhang, P. Liu, B. Xu, B. Zhang, H. Chen, A. K. Inge, Y. Li, H. Wang, Y.-B. Cheng, L. Kloo and L. Sun, *Chem. Commun.*, 2018, **54**, 9571–9574.
10 J. Burschka, A. Dualeh, F. Kessler, E. Baranoff, N. L. Cevey-Ha, C. Yi, M. K. Nazeeruddin and M. Gratzel, *J. Am. Chem. Soc.*, 2011, **133**, 18042–18045.
11 A. Abate, D. J. Hollman, J. Teuscher, S. Pathak, R. Avolio, G. D'Errico, G. Vitiello, S. Fantacci and H. J. Snaith, *J. Am. Chem. Soc.*, 2013, **135**, 13538–13548.
12 B. Xu, J. Huang, H. Ågren, L. Kloo, A. Hagfeldt and L. Sun, *ChemSusChem*, 2014, **7**, 3252–3256.
13 L. Caliò, M. Salado, S. Kazim and S. Ahmad, *Joule*, 2018, **2**, 1800–1815.
14 M. Namatame, M. Yabusaki, T. Watanabe, Y. Ogomi, S. Hayase and K. Marumoto, *Appl. Phys. Lett.*, 2017, **110**, 123904.
15 S. Fantacci, F. De Angelis, M. K. Nazeeruddin and M. Grätzel, *J. Phys. Chem. C*, 2011, **115**, 23126–23133.
16 B. Xu, J. Zhang, Y. Hua, P. Liu, L. Wang, C. Ruan, Y. Li, G. Boschloo, E. M. J. Johansson, L. Kloo, A. Hagfeldt, A. K. Y. Jen and L. Sun, *Chem*, 2017, **2**, 676–687.
17 C. Chen, W. Zhang, J. Cong, M. Cheng, B. Zhang, H. Chen, P. Liu, R. Li, M. Safdari, L. Kloo and L. Sun, *ACS Energy Lett.*, 2017, **2**, 497–503.
18 D. Shi, X. Qin, Y. Li, Y. He, C. Zhong, J. Pan, H. Dong, W. Xu, T. Li, W. Hu, J.-L. Brédas and O. M. Bakr, *Sci. Adv.*, 2016, **2**, e1501491.
19 B. Shen, Z. Hu, H. Xu, K. Sun, S. Feng, J. Zhang and Y. Zhu, *Cryst. Growth Des.*, 2019, **19**, 3272–3278.
20 W. H. Nguyen, C. D. Bailie, E. L. Unger and M. D. McGehee, *J. Am. Chem. Soc.*, 2014, **136**, 10996–11001.
21 U. Bach, *Solid-state dye-sensitized mesoporous TiO_2 Solar Cells*, PhD thesis, Lausanne, EPFL, 2000, DOI: 10.5075/epfl-thesis-2187.
22 T. Chu and Y. Liu, *Org. Electron.*, 2018, **53**, 165–184.
23 W. Zhang, P. Liu, A. Sadollahkhani, Y. Li, B. Zhang, F. Zhang, M. Safdari, Y. Hao, Y. Hua and L. Kloo, *ACS Omega*, 2017, **2**, 9231–9240.
24 B. Tan, S. R. Raga, A. S. R. Chesman, S. O. Fürer, F. Zheng, D. P. McMeekin, L. Jiang, W. Mao, X. Lin, X. Wen, J. Lu, Y. B. Cheng and U. Bach, *Adv. Energy Mater.*, 2019, **9**, 1901519.

